




# Analyzing the electron trajectories in strong-field tunneling ionization with the phase-of-the-phase spectroscopy

JIA TAN,<sup>1,2</sup> YUEMING ZHOU,<sup>1,5</sup> SHENGLIANG XU,<sup>1,3</sup> QINGHUA KE,<sup>1</sup>  
JINTAI LIANG,<sup>1</sup> XIAOMENG MA,<sup>4</sup> WEI CAO,<sup>1</sup> MIN LI,<sup>1</sup>  QINGBIN  
ZHANG,<sup>1</sup> AND PEIXIANG LU<sup>1,3,6</sup>

<sup>1</sup>Wuhan National Laboratory for Optoelectronics and School of Physics, Huazhong University of Science and Technology, Wuhan 430074, China

<sup>2</sup>Jiangsu Key Laboratory of Micro and Nano Heat Fluid Flow Technology and Energy Application, School of Physical Science and Technology, Suzhou University of Science and Technology, Suzhou, 215009, China

<sup>3</sup>Laboratory of Optical Information Technology, Wuhan Institute of Technology, Wuhan 430205, China

<sup>4</sup>Department of Physics and Mechanical and Electrical Engineering, Hubei University of Education, Wuhan 430205, China

<sup>5</sup>zhouymhust@hust.edu.cn

<sup>6</sup>lupeixiang@hust.edu.cn

**Abstract:** By numerically solving the time-dependent Schrödinger equation, we theoretically study strong-field tunneling ionization of Ar atom in the parallel two-color field which consists of a strong fundamental pulse and a much weaker second harmonic component. Based on the quantum orbits concept, we analyzed the photoelectron momentum distributions with the phase-of-the-phase spectroscopy, and the relative contributions of the two parts of the photoelectrons produced during the rising and falling edges of the adjacent quarters of the laser cycle are identified successfully. Our results show that the relative contributions of these two parts depend on both of the transverse and longitude momenta. By comparing the results from model atoms with Coulomb potential and short-range potential, the role of the long-range Coulomb interaction on the relative contributions of these two parts of electrons is revealed. Additionally, we show that the effects of Coulomb interaction on ionization time are vital for identifying their relative contributions.

© 2021 Optical Society of America under the terms of the [OSA Open Access Publishing Agreement](#)

## 1. Introduction

Laser-induced tunneling ionization of atoms and molecules is one of the most fundamental processes in strong-field laser-matter interaction, and it serves as the first step of a broad range of strong-field phenomena, such as above-threshold ionization (ATI) [1,2], high-order harmonic generation [3,4], and non-sequential double ionization [5–7]. In past decades, these strong-field phenomena have been widely studied, and their applications in the attosecond community have been extensively exploited, including attosecond pulse generation [8–11], molecular tomography [12,13], and probing ultrafast electronic and nuclear dynamics [14–16]. In these studies, the trajectory-based concept is of basic importance [17]. Generally, in the trajectory-based concept these ultrafast processes could be understood in terms of three-step model [18], wherein the electron is first tunneling ionized through the potential barrier, and then the released electron wave packet (EWP) is accelerated by the oscillating electric field of the laser pulse. Part of the EWP may return back to scatter or recombine with the atomic or molecular core, while the other part reaches to the detector directly. Thorough and comprehensive knowledge about the electron trajectories is crucially important for further performing the applications of these phenomena [19–26]. In the past years, great efforts have been made in revealing the details of the trajectory

picture. For example, numerous studies have been reported in characterizing the tunneling of the EWP, i.e., the first step of the electron trajectory. The tunneling ionization time [27,28], the tunneling exit point [29], and the phase of tunneling EWP were hence accurately explored [30,31].

An important issue in the trajectory-based picture is that different trajectories could contribute to the same final observation [17,32,33]. For example, in the photoelectron momentum distribution (PEMD) of tunneling ionization, electron released at different times of the laser pulse could reach the same final momentum [32]. Specifically, within one laser cycle, the so-called long and short trajectories, which are respectively generated during the descending and ascending edges of the adjacent quarters of the laser field, possess the same final momentum [34,35]. Due to the effects of the Coulomb rescattering on the long trajectory, it is commonly accepted that the electrons produced from the long trajectory dominate the contributions of the PEMD, especially for the distribution along the laser polarization direction. In recent experimental studies [36], the electron trajectories in strong-field tunneling ionization have been analyzed. With the assumption that only the long trajectory contributes to the PEMDs, the reconstructed ionization time deviates seriously from theoretical prediction based on the Coulomb-corrected strong-field approximation. We should mention that in the previous researches, the accuracy of the Coulomb-corrected strong-field approximation model in describing the ionization has been approved [37–41]. Therefore, the non-negligible contributions of the short trajectory may be responsible for the discrepancy [42]. Identifying the contributions of these two trajectories is necessary for the time-resolved measurement based on the photoelectron spectroscopy.

In a recent study [43,44], with the orthogonally polarized two-color field the relative contributions of the long and short trajectories have been explored. It was shown that although the electrons from the long trajectory have high contributions, and the contributions of short trajectory are also significant. In that study, the relative contributions of the long and short trajectories are identified for the PEMD along the polarization direction of the fundamental field ( $p_y = 0$ ) and the line of non-zero lateral momentum  $p_z$  but keeping  $p_y = 0$ . The effects of the Coulomb interaction on the ionization time were not considered when identifying the relative contributions, which may influence the conclusions.

In this paper, we reveal the relative contributions of the long and short trajectories in the whole space of the PEMDs with the parallel two-color (PTC) field. The recently developed phase-of-the-phase spectroscopy is employed to analyze these PEMDs [45–50]. In this method, the relative phase of the two-color field is continually changed, and the photoelectron yield at each momentum is monitored as a function of the relative phase. The trajectories generated from different times have different dependence on the relative phase of the two-color field. Thus, the dependence of the photoelectron yield on the relative phase revealed by the phase-of-the-phase spectroscopy could provide information about the electron trajectories. This method has been applied to the parallel two-color field, orthogonal two-color field as well as the circularly polarized two-color field [36,47,51,52]. Based on this method, the dynamics of strong-field ionization in the tunneling [47] and multi-photon regimes [53] have been revealed, the multiple rescattering trajectories in tunneling ionization have been resolved [54], and the structural information of the atoms and molecules have also been explored [47]. Very recently, it has been employed to retrieve the temporal properties of the fork structure in the PEMDs [55]. Here, the long and short trajectories are generated during the adjacent quarter cycles of the laser pulse through tunneling ionization, and thus the photoelectron yields depend differently on the relative phase of the two-color field. By analyzing this phase dependence of PEMDs, the relative contributions of the two trajectories could be obtained.

In our work, the laser field is consisted by a strong 1600nm fundamental component and a weak second harmonic component. The PEMDs are obtained by solving the time-dependent Schrödinger equation for different relative phases, from which the phase-of-the-phase spectrum

is extracted. Analyzing the phase-of-the-phase spectrum together with the Coulomb-corrected strong field approximation, the relative contributions of the electrons from the long and short trajectories in strong-field tunneling ionization are disentangled quantitatively. The results show that their relative contributions depend on the transverse and longitude momenta. Additionally, applying the scheme for model atom with short-range potential, it is observed the momentum dependence of the relative contributions becomes much weaker. This is because that the long-range Coulomb potential significantly changes the momentum distribution of the rescattering electron. Owing to the holographic interference induced by the coherent superposition of the direct and rescattering electrons, the contributions of the long trajectory are greatly suppressed or enhanced at the interference minima and maxima. Furthermore, our work shows that the effect of the Coulomb interaction on the ionization time can not be ignored in the scheme and it is vital for identifying the different trajectories.

## 2. Theoretical method

In our calculation, the parallel two-color (PTC) laser field  $\mathbf{E}(t)$  is combined by a strong 1600-nm fundamental (FM) field  $\mathbf{E}_1(t)$  and a perturbative second harmonic (SH) component  $\mathbf{E}_2(t)$ , which is written as

$$\begin{aligned}\mathbf{E}(t) &= \mathbf{E}_1(t) + \mathbf{E}_2(t) \\ &= -f(t)[E_1 \cos(\omega_1 t) + E_2 \cos(\omega_2 t + \varphi)]\hat{x},\end{aligned}\quad (1)$$

where  $\hat{x}$  denotes the polarization direction of the two-color laser field.  $f(t)$  indicates the trapezoidal envelop, which ramps on and off over one optical cycle with a plateau of eight periods of the FM field.  $\omega_1$  and  $\omega_2$  are the frequencies of the FM and SH components, and  $E_1$  and  $E_2$  indicate their corresponding electric field amplitudes, respectively.  $\varphi$  represents the relative phase between the PTC laser field. The laser intensities of the FM and SH components are  $1.2 \times 10^{14}$  W/cm<sup>2</sup> and  $1.2 \times 10^{11}$  W/cm<sup>2</sup>, respectively.

### 2.1. Numerically solving the time dependent Schrödinger equation

In the above PTC laser field, we numerically solve the two-dimensional time-dependent Schrödinger equation (TDSE) within dipole approximation. In the length gauge, the TDSE is given by [Atomic units (a.u.) are used throughout unless stated otherwise.]

$$i\frac{\partial\Psi(\mathbf{r},t)}{\partial t} = H(\mathbf{r},t)\Psi(\mathbf{r},t),\quad (2)$$

where  $\Psi(\mathbf{r},t)$  represents the wave function,  $\mathbf{r}$  denotes the electron coordinate in the polarization plane of the PTC field and  $H(\mathbf{r},t) = -\frac{1}{2}\nabla^2 + V(\mathbf{r}) + \mathbf{r} \cdot \mathbf{E}(t)$  is the Hamiltonian. In the Hamiltonian, the long-range Coulomb potential for Ar atom is written as  $V(\mathbf{r}) = -1/\sqrt{x^2 + y^2 + \eta}$  (with the ionization potential  $I_p = 0.58$  a.u.), where the soft-core parameter  $\eta$  is set to be 0.39. For the model atom with short-range potential, the binding potential is given by

$$V(\mathbf{r}) = -\frac{1}{\sqrt{x^2 + y^2 + a}} \cdot e^{-\frac{x^2+y^2}{s^2}},\quad (3)$$

where  $s$  is the screening parameter. For different  $s$ , the soft-core parameter  $a$  is adjusted to reproduce the ionization potential of Ar.

The initial ground state is prepared by the imaginary-time propagation [56], and the wave function  $\Psi(\mathbf{r},t)$  is propagated with the splitting-operator method in real time [57]. Due to the linearity of the Schrödinger equation, we divide the whole wave function for the real-time propagation into two regions smoothly: the inner region ( $0 - R_s$ ) and the outer region ( $R_s - R_{max}$ )

by a splitting function [58]. At any given time  $\tau$ , the electron wave function  $\Psi(\tau)$  is given by [58,59]

$$\begin{aligned}\Psi(\tau) &= \Psi(\tau)[1 - F_s(R_s)] + \Psi(\tau)F_s(R_s) \\ &= \Psi_I(\tau) + \Psi_{II}(\tau).\end{aligned}\quad (4)$$

Here,  $F_s(R_s) = 1/[1 + e^{-(r-R_s)/\Delta}]$  is the splitting function,  $\Delta$  represents the width of the crossover region and  $R_s$  is the boundary of the inner space [60]. In the inner space, the wave function  $\Psi_I$  propagates under the full Hamiltonian. In the outer space, the wave function  $\Psi_{II}$  stands for the "ionized part" and it analytically propagates under the Volkov Hamiltonian. More specifically, at each time step, the wave function  $\Psi_{II}$  in the outer region is firstly transformed into the momentum space,

$$C(\mathbf{p}, \tau) = \int \Psi_{II}(\mathbf{r}, \tau) \frac{e^{-i[\mathbf{p}+\mathbf{A}(\tau)]\cdot\mathbf{r}}}{2\pi} d^2\mathbf{r}, \quad (5)$$

where  $\mathbf{A}(\tau) = -\int_{-\infty}^{\tau} \mathbf{E}(t)dt$  is the laser vector potential. Then, it is propagated from this moment  $\tau$  to the end of the laser pulse, using

$$\Psi(\infty, \tau) = \int \bar{C}(\mathbf{p}, \tau) \frac{e^{i\mathbf{p}\cdot\mathbf{r}}}{2\pi} d^2\mathbf{p} \quad (6)$$

with  $\bar{C}(\mathbf{p}, \tau) = e^{-i\int_{\tau}^{\infty} \frac{1}{2}[\mathbf{p}+\mathbf{A}(\tau')]^2 d\tau'} C(\mathbf{p}, \tau)$ . Finally, the PEMD is obtained by summing the wave function

$$\frac{dP(\mathbf{p})}{dEd\theta} = \sqrt{2E} \left| \sum_{\tau} \bar{C}(\mathbf{p}, \tau) \right|^2 \quad (7)$$

over the time  $\tau$ . Here,  $\mathbf{p}$  denotes the electron final momentum,  $E = \mathbf{p}^2/2$  is the electron energy, and  $\theta$  indicates the electron emission angle.

In the calculations, the Cartesian grid ranges from -700 a.u. to 700 a.u. for both  $x$  and  $y$  directions with a grid size of  $\Delta x = \Delta y = 0.34$  a.u. The boundary of the inner space  $R_s$  is set to be 200 a.u. with the width of crossover region  $\Delta = 8$  a.u. It should be mentioned that enlarging the value of the boundary  $R_c$  will not induce visible difference in the PEMDs. Therefore, the turning off of the Coulomb potential in the region of  $r > 200$  a.u. will not affect our final results. The propagation time step of the wave function is fixed at  $\Delta t = 0.2$  a.u. Moreover, at the end of the laser pulse, the wave function is propagated for two additional optical cycles of the laser pulse to make sure that the "slow" electrons exceed the boundary of the inner space  $R_s$  [61].

## 2.2. Strong-field approximation

To identify the contributions of the long and short trajectories in PEMDs, we resort to the strong-field approximation (SFA) in the length gauge [17,62]. In SFA, the ionization amplitude of photoelectron, from a initial ground state to a final state with the final momentum  $\mathbf{p}$ , is expressed as  $|\Gamma|^2 \propto \rho_s(\mathbf{p}; t_j) e^{-2\text{Im}[\Phi(\mathbf{p}; t_j)]}$  [63], where  $t_j$  represents the ionization time of the electron trajectory  $j$ . With the SFA, we calculate the tunneling ionization probabilities for the long and short trajectories separately. We are interested in the relative change of the ionization amplitude in the PTC field, and thus the pre-exponential factor  $\rho_s(\mathbf{p}, t_j)$ , which is insensitive to the perturbation of the SH field, is ignored here. The classical action is accumulated by

$$\Phi(\mathbf{p}; t_j) = - \int_{t_j}^{t_f} [\mathbf{v}(t)^2/2 + I_p] dt, \quad (8)$$

where  $\mathbf{v}(t) = \mathbf{p} + \mathbf{A}(t)$  denotes the instantaneous momentum of electron, and  $t_f$  is the pulse turn-off time. In the PTC field that we adopted, the SH component is much weaker than the FM

field (lower than 1%) and thus it can be treated as a small perturbation. Because the tunneling rate depends exponentially on the strength of electric field, this perturbation could affect the tunneling rate, but it does not affect the final momentum of photoelectron (The momentum change in the PTC field can be estimated to be  $\mathbf{A}_2$ , where  $\mathbf{A}_2$  is the vector potential of the SH field). So, by monitoring the changes of photoelectron yield at fixed momentum, we could resolve the contributions of different trajectories. This is essential in our scheme. Therefore, the ionization time  $t_j$  of PTC field which corresponds to the electron final momentum can be approximately governed by the saddle-point equation (SPE) in the FM field [64] i.e.,

$$[\mathbf{p} + \mathbf{A}_1(t_j)]^2/2 + I_p = 0, \quad (9)$$

where  $\mathbf{A}_1$  represents the vector potential of the FM field.

According to Eq. (8), the relative change of the ionization amplitude in the PTC field with respect that in the FM field is expressed as

$$\begin{aligned} \Delta Y(\mathbf{p}; t_j; \varphi) &= |\Gamma^{\text{PTC}}(\mathbf{p}; t_j; \varphi)|^2 - |\Gamma^{\text{FM}}(\mathbf{p}; t_j)|^2 \\ &\propto e^{-2\text{Im}[\Phi^{\text{PTC}}(\mathbf{p}; t_j)]} - e^{-2\text{Im}[\Phi^{\text{FM}}(\mathbf{p}; t_j)]} \\ &= e^{-2\text{Im}\{-\int_{t_j}^{t_f} \{[\mathbf{p} + \mathbf{A}_1(t) + \mathbf{A}_2(t)]^2/2 + I_p\} dt\}} - e^{-2\text{Im}\{-\int_{t_j}^{t_f} \{[\mathbf{p} + \mathbf{A}_1(t)]^2/2 + I_p\} dt\}} \\ &= e^{-2\text{Im}[\Phi^{\text{FM}}(\mathbf{p}; t_j)]} \{e^{-2\text{Im}[\Delta\Phi(\mathbf{p}; t_j; \varphi)]} - 1\}, \end{aligned} \quad (10)$$

where  $\Phi^{\text{FM}}(\mathbf{p}; t_j) = -\int_{t_j}^{t_f} \{[\mathbf{p} + \mathbf{A}_1(t)]^2/2 + I_p\} dt$  and  $\Phi^{\text{PTC}}(\mathbf{p}; t_j) = -\int_{t_j}^{t_f} \{[\mathbf{p} + \mathbf{A}_1(t) + \mathbf{A}_2(t)]^2/2 + I_p\} dt$  indicate the classical actions of electron in the FM and PTC fields, respectively. The complex phases difference  $\Delta\Phi(\mathbf{p}; t_j; \varphi)$  is obtained by

$$\Delta\Phi(\mathbf{p}; t_j; \varphi) = -\int_{t_j}^{t_f} [\mathbf{p} + \mathbf{A}_1(t)]\mathbf{A}_2(t; \varphi) dt. \quad (11)$$

In Eq. (11),  $\int_{t_j}^{t_f} \mathbf{A}_2(t; \varphi)^2/2 dt$  is a high-order perturbation, and thus it is approximately dropped. Equation (11) indicates that the relative change of the ionization amplitude is a function of the relative phase. The phase-of-the-phase  $\varphi_m$ , where the ionization signal maximizes, depends on the ionization time  $t_j$  and can be determined by

$$\partial\text{Im}[\Delta\Phi(\mathbf{p}; t_j; \varphi)]/\partial\varphi = 0. \quad (12)$$

### 2.3. Coulomb-corrected strong-field approximation

We should mention that in the SFA, the Coulomb interaction of the electron and parent ion has not been taken into account, thus the correspondence between the final momentum and ionization time is inaccurate. In previous studies, it has been demonstrated that the Coulomb-corrected SFA can depict the photoelectron momentum map precisely [37–41]. Here, to include the influences of Coulomb interaction properly, we employ the Coulomb-corrected SFA. In the FM field, the Coulomb force caused by the parent ion is inserted into the electronic motion equation,

$$\ddot{\mathbf{r}} = d\mathbf{v}/dt = -\mathbf{E}_1 - \nabla V(\mathbf{r}). \quad (13)$$

When the ionized electron propagates under the potential barrier, the complex phase  $\Phi_{\text{sub}}(t_j) = -\int_{t_j}^{\text{Re}[t_j]} [\mathbf{v}^2/2 + I_p + V(\mathbf{r})] dt$  of each trajectory is evaluated from the saddle point time  $t_j$  to its real part. After electron tunnels from the barrier, it is governed by  $\Phi_{\text{prop}}(t_j) = -\int_{\text{Re}[t_j]}^{t_f} [\mathbf{v}^2/2 + I_p + V(\mathbf{r})] dt$ , until the laser pulse turns off. Finally, the asymptotic momentum  $\mathbf{p}$  of the electron

on the detector is calculated by Kepler's laws [65]. In Eq. (9),  $\mathbf{p}$  is conserved, i.e.,  $\dot{\mathbf{p}} = 0$ . Here, it is no longer a constant, and is replaced by  $\dot{\mathbf{p}} = -\nabla V(\mathbf{r})$ . Thus, the correspondence between  $\mathbf{p}$  and the saddle-point time is modified, as it satisfies

$$[\mathbf{p} + \mathbf{A}_1(t_j')]^2/2 + I_p = 0. \quad (14)$$

Accordingly, the Eq. (10) is rewritten as

$$\Delta Y(\mathbf{p}; t_j'; \varphi) \propto e^{-2\text{Im}[\Phi^{\text{FM}}(\mathbf{p}; t_j')]} \{e^{-2\text{Im}[\Delta\Phi(\mathbf{p}; t_j'; \varphi)]} - 1\}. \quad (15)$$

### 3. Result and discussion

Figures 1(a)–1(c) illustrate the PEMDs for strong-field tunneling ionization of Argon atom obtained by numerically solving TDSE. Figure 1(a) displays the result of 1600-nm single-color laser field, and Figs. 1(b) and 1(c) display the results of the PTC laser field with relative phases  $\varphi = 0$ , and  $\pi$ , respectively. The PTC field is polarized along  $x$  direction and it consists of a 1600-nm FM field and an 800-nm field with the laser intensities of  $1.2 \times 10^{14}$  W/cm<sup>2</sup> and  $1.2 \times 10^{11}$  W/cm<sup>2</sup>, respectively. From these PEMDs, one can see three types of interference fringes. The first one, centered around zero momentum in the PEMDs, presents as the ring-like structure. It known as the ATI peaks is the inter-cycle interference [66,67]. The second one, manifested nearly horizontal fringes, is referred as the strong photoelectron holographic pattern [39,64]. This type of interference has been broadly studied very recently, and it has been applied to probe the structure and ultrafast electron dynamics in atoms and molecules [16,30,68,69]. The third type of the interference exhibits the nearly vertical fringes and is most visible on the  $p_x$  axis. It results from the coherent superposition of the two types of trajectories that are produced during the two adjacent quarter cycles of the laser pulse [34,35]. These two trajectories are called as long and short trajectories, respectively. For a multiple-cycle laser pulse, the ionization amplitudes of these two types of trajectory are exactly the same if no Coulomb interaction after tunneling is involved. However, due to the long-range Coulomb potential, which are different for the long and short trajectories, their contributions in the PEMDs are thus different. Accurate knowledge about the relative contributions is necessary for the information retrieval from the PEMDs. So, our goal is to identify the relative contributions of these two trajectories. In the following, we will show that by applying the recently proposed phase-of-the-phase spectrum, the relative contributions of the electrons released during the adjacent half cycles of the laser pulse in strong-field tunneling ionization can be disentangled quantitatively.

For comparison, we also show the PEMDs by calculating TDSE for Ar atom with the short-range potential of Eq. (3). In Figs. 1(d)–1(f), we show the results for the short-range potential with  $s = 1$ . Compared to the results of Figs. 1(a)–1(c), it is clear that the holographic interference structure fades out. This is because that the nearly forward rescattering, which is responsible for the holographic pattern, is strongly suppressed in the short-range potential [70], [71].

To apply the phase-of-the-phase spectrum, we calculate the PEMDs by changing the relative phase  $\varphi$  of the two-color field from 0 to  $2\pi$  in the step of  $0.05\pi$ . The PEMDs change correspondingly, as shown in Fig. 1. Because the intensity of the SH in our two-color field is three orders of magnitude weaker than the FM field, the changes of the PEMDs with the relative phase are very perturbative. To show the effects of the SH on the PEMDs more clearly, we then calculate the normalized difference (ND) of the PEMDs [30]. The NDs are defined as

$$\text{ND}(\mathbf{p}; \varphi) = \frac{Y(\mathbf{p}; \varphi) - Y_{\text{avg}}(\mathbf{p})}{Y(\mathbf{p}; \varphi) + Y_{\text{avg}}(\mathbf{p})}, \quad (16)$$

where  $Y(\mathbf{p}; \varphi)$  denotes the PEMD at the relative phase of  $\varphi$ , and  $Y_{\text{avg}}(\mathbf{p}; \varphi)$  indicates the average of the PEMDs for  $\varphi$  ranging from 0 to  $2\pi$ . Figures 2(a) and 2(b) display two examples of the NDs

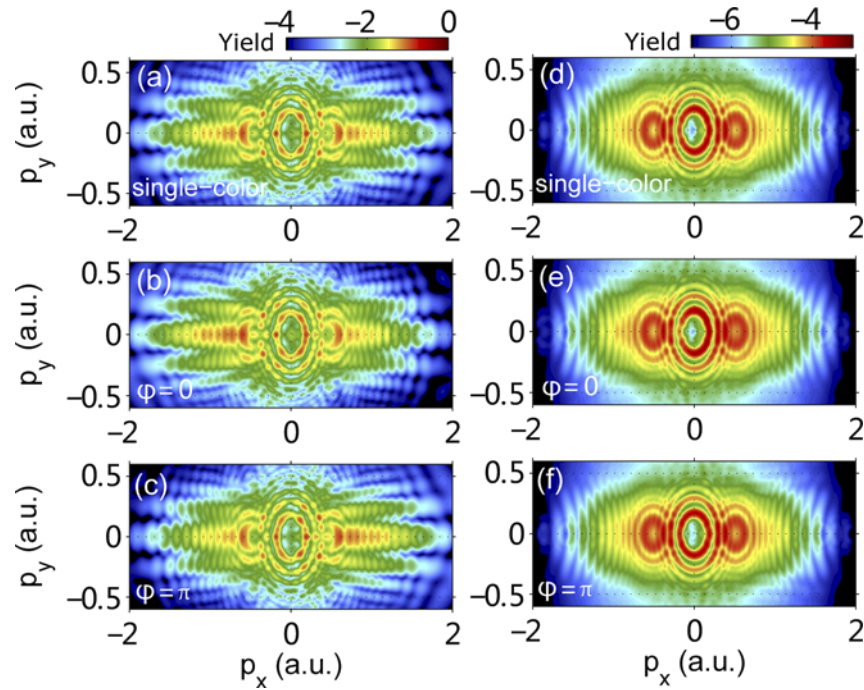


**Fig. 1.** (a)-(c) The PEMDs of Ar obtained by solving the TDSE for the 1600-nm single-color field and the PTC field with relative phases  $\varphi = 0$  and  $\pi$ , respectively. (d)-(f) Same as (a)-(c) but for the model atom with the short-range potential ( $s = 1$ ). The color bar of these PEMDs are in logarithm scale.

for the Coulomb potential at  $\varphi = 0$  and  $\pi$ , respectively. Figures 2(e) and 2(f) show the results for the short-range potential with  $s = 1$ . Clearly, the dependence of the photoelectron yields on the relative phase can be seen. For instance, the NDs are nearly antisymmetry about  $p_x = 0$ . At  $\varphi = 0$ , the NDs are almost negative and positive for  $p_x > 0$  and  $p_x < 0$ , respectively. While, at  $\varphi = \pi$ , the situation is reversed. For the short-range potential, the NDs are very close to zero. We should mention that at other relative phases, the anti-symmetry of NDs can also be observed.

The  $\text{ND}(\mathbf{p}; \varphi)$  indicates that the photoelectron yield at each momentum has been modulated by the weak SH field. The phase-of-the-phase spectroscopy is proposed to characterize this modulation. We apply this spectroscopy to the NDs. For the weak SH field, the modulation of the photoelectron yield on the relative phase  $\varphi$  at each momentum could be described by

$$\text{ND}(\mathbf{p}; \varphi) = P(\mathbf{p}) \cos[\varphi - \varphi_m(\mathbf{p})], \quad (17)$$

where  $P(\mathbf{p})$  indicates the amplitude of the modulation and  $\varphi_m(\mathbf{p})$  denotes the relative phase where NDs maximize. Technically, these two quantities can be obtained by Fourier transforming of NDs with respect to  $\varphi$  at each momentum  $\mathbf{p}$  as well. Figures 2(c) and 2(g) show the obtained  $\varphi_m$  at each momentum  $\mathbf{p}$ . For a better view, several cuts of  $\varphi_m$  are displayed in Figs. 2(d) and 2(h). Due to the symmetry, we only consider the region of  $p_x < 0$  in the following. It is shown that in Fig. 2(d) the phase  $\varphi_m$  oscillates between  $1.5\pi$  and  $1.8\pi$  for the cut at  $p_x = -0.8$  a.u.. The amplitude of this oscillation depends on  $p_x$ . For the short-range potential with  $s = 1$ , the obtained  $\varphi_m$  is located near  $1.5\pi$  for the momentum range  $|p_y| < 0.4$  a.u. and the oscillation is much weaker. When the Coulomb interaction range increases ( $s = 10$ ), the results get closer to the data of Coulomb potential corresponding to infinite  $s$ . The obtained  $\varphi_m$  contains the information about

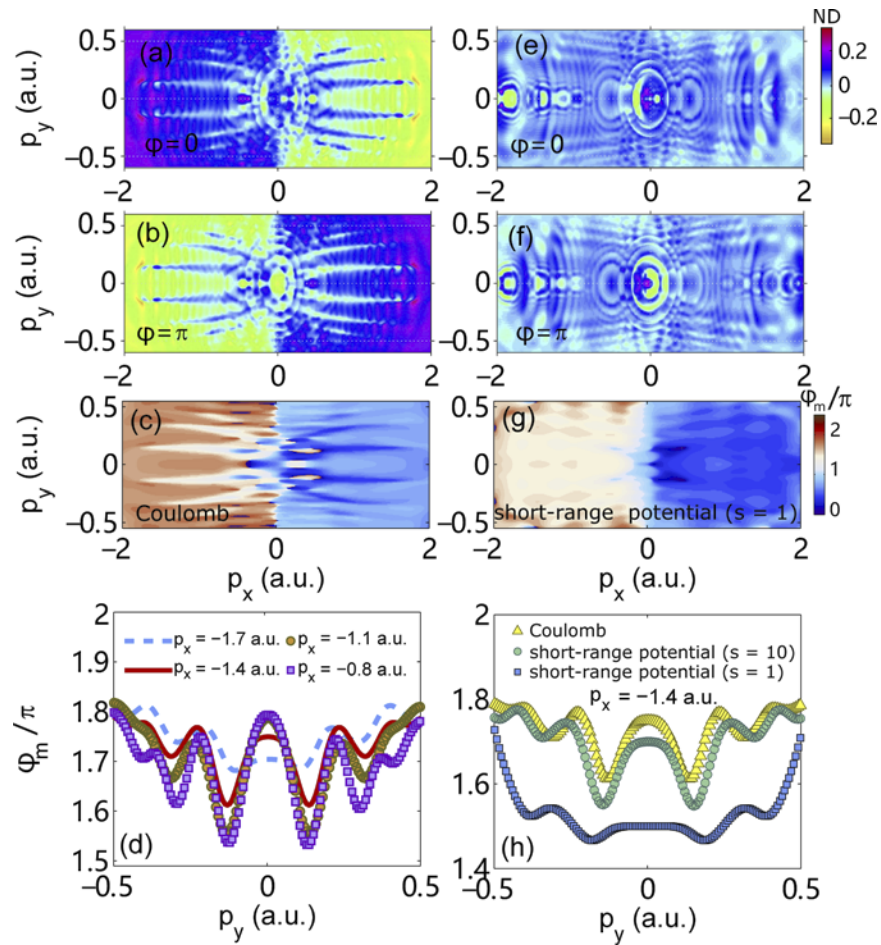


**Fig. 2.** (a)-(b) The corresponding NDs extracted from Figs. 1(b)–1(c), respectively. (c) The phase-of-the-phase spectrum for the Coulomb potential. (d) Several cuts of the phase-of-the-phase spectrum from (c) at  $p_x = -0.8$  a.u. (purple squares),  $-1.1$  a.u. (yellow circles),  $-1.4$  a.u. (solid red curve) and  $-1.7$  a.u. (dashed blue curve). (e)-(f) The corresponding NDs extracted from Figs. 1(e)–1(f), respectively. (g) The phase-of-the-phase spectrum for the short-range potential with  $s = 1$ . (h) Cuts of the phase-of-the-phase spectrum at  $p_x = -1.4$  a.u. for the Coulomb potential (yellow triangles), and the short-range potentials with  $s = 1$  (blue squares) and  $s = 10$  (green circles).

the relative contributions of the long and short trajectories. In the below calculations, we will extract this information.

Figure 3(a) illustrates the corresponding time windows of the long and short trajectories, and Fig. 3(b) shows the schematic of these corresponding trajectories. The ionization of the electron from short trajectory occurs at the ascending edge of the FM field. For this type of trajectories, the electrons drift to the detector directly after tunneling. For the long trajectory, the electrons are released during the descending edge of the FM field. Driven by the laser field, their directions are reversed and the electrons return back to the parent ion. Owing to the effects of the Coulomb interaction, part of the returning electrons may undergo re-collision with the parent ion before reaching to the detector. The rescattering probability of electron is proportional to the differential scattering cross section  $\sigma(p'; \theta)$ , and for the Coulomb potential, it can be written as (in the first



Born approximation)

$$\sigma(p'; \theta) = \frac{1}{4p'^4 \sin^4 \theta/2}, \quad (18)$$

where  $p'$  represents the incident momentum and  $\theta$  indicates the scattering angle. This indicates that for the momentum region we consider here (within  $2U_p = 2.1$  a.u., where  $U_p = E_1^2/4\omega_1^2$  is the ponderomotive energy of the FM field), the rescattering probability of the electron scattered with a large angle (where  $|\theta|$  is much larger than  $\pi/2$ ) is much less than that of near-forward rescattering electron (where  $|\theta|$  is much less than  $\pi/2$ ), and thus the re-collision is mainly soft re-collision. With the SFA we separately calculate the photoelectron yields for the short and long trajectories as functions of the relative phase of the PTC field. The obtained NDs for the direct electron of long and short trajectories at  $p_y = 0$  are shown in Figs. 3(c) and 3(d), respectively. Note that the NDs periodically oscillate with relative phase of the two-color field, and the period of oscillation is  $2\pi$ . Thus, for better view, we show the NDs ranging from  $\pi$  to  $3\pi$ . From Figs. 3(c) and 3(d), it can be clearly observed that the obtained phase  $\varphi_m$  sensitively depends on the longitudinal momentum  $p_x$ . Moreover, for the short and long trajectories these dependence are different. For example, for the short trajectory,  $\varphi_m$  of the direct electron decreases from  $1.4\pi$  to  $\pi$  as  $p_x$  increases. While for the long trajectory,  $\varphi_m$  increases gradually from  $1.6\pi$  to  $2\pi$  as  $p_x$  increases.

In our PTC fields, the relative phase where the yield of the photoelectron at momentum  $\mathbf{p}$  maximizes is closely related to the ionization times of electrons, as indicated by Eq. (12). Specifically, for the direct electron at  $p_y = 0$ , we have  $p_x = -\text{Re}[\mathbf{A}_1(t_j)]$ , and thus the relationship between the phase  $\varphi_m$  and ionization times could be briefly described in terms of  $\varphi_m = -3\omega_1 \text{Re}[t_j]/2$  [42]. For the direct electron of long and short trajectories, the electrons are produced from the adjacent quarter cycles of the laser pulse. Therefore, the photoelectron yields depend differently on the relative phase of the two-color field, as shown in Figs. 3(c) and 3(d). Note that for the momentum region we focus on, the final traverse momentum of the soft-recollision electron (near-forward rescattering electron) from the long trajectory is small. According to the SPEs, the ionization times of the direct and the near-forward rescattering electrons are almost the same (their ionization time differences are well below 0.5 a.u.) [28]. This implies that their relative phase dependence on photoelectron yield and the phase  $\varphi_m$  are also the same, as demonstrated in Fig. 3(c). So, we can classify the trajectories of direct and near-forward rescattering electrons into the same trajectory, and in our phase-of-the-phase analysis only the ionization time of the direct electron is required. In the followings, we employ  $\varphi_m^L$  to express  $\varphi_m$  of the long trajectory, and use  $\varphi_m^S$  to indicate that of the short trajectory. As displayed by the black arrow of Fig. 3(d), a natural phase window is hence formed between  $\varphi_m^L$  and  $\varphi_m^S$ . For each  $\mathbf{p}$ , we repeat the calculations of the phase-of-the-phase spectra for the long and short trajectories. The obtained results are shown in Figs. 3(e)–3(f).

For the PEMDs in strong-field tunneling ionization, both of the long and the short trajectories have significant contributes. The ionization amplitude of photoelectron with final momentum  $\mathbf{p}$  can expressed as the coherent superposition of long and short trajectories,

$$\begin{aligned} |\Gamma^{\text{PTC}}(\mathbf{p}; \varphi)|^2 &= |\sqrt{\alpha}\Gamma^L(\mathbf{p}; \varphi) + \sqrt{\beta}\Gamma^S(\mathbf{p}; \varphi)|^2 \\ &= \alpha|\Gamma^L(\mathbf{p}; \varphi)|^2 + \beta|\Gamma^S(\mathbf{p}; \varphi)|^2 \\ &\quad + 2\sqrt{\alpha}\sqrt{\beta}|\Gamma^L(\mathbf{p}; \varphi)||\Gamma^S(\mathbf{p}; \varphi)|\cos(\delta\theta). \end{aligned} \quad (19)$$

Here,  $|\Gamma^L(\mathbf{p}; \varphi)|^2$  and  $|\Gamma^S(\mathbf{p}; \varphi)|^2$  indicate the ionization amplitudes of the long and short trajectories, respectively.  $\alpha$  and  $\beta$  characterize their contributions.  $\delta\theta$  is the phase difference between the long and short trajectories. Due to the laser focal volume effect, the interference pattern formed by the electron of long and short trajectories is smeared out, and thus the interference term is safely canceled here. Specifically, as shown above, the ionization amplitudes

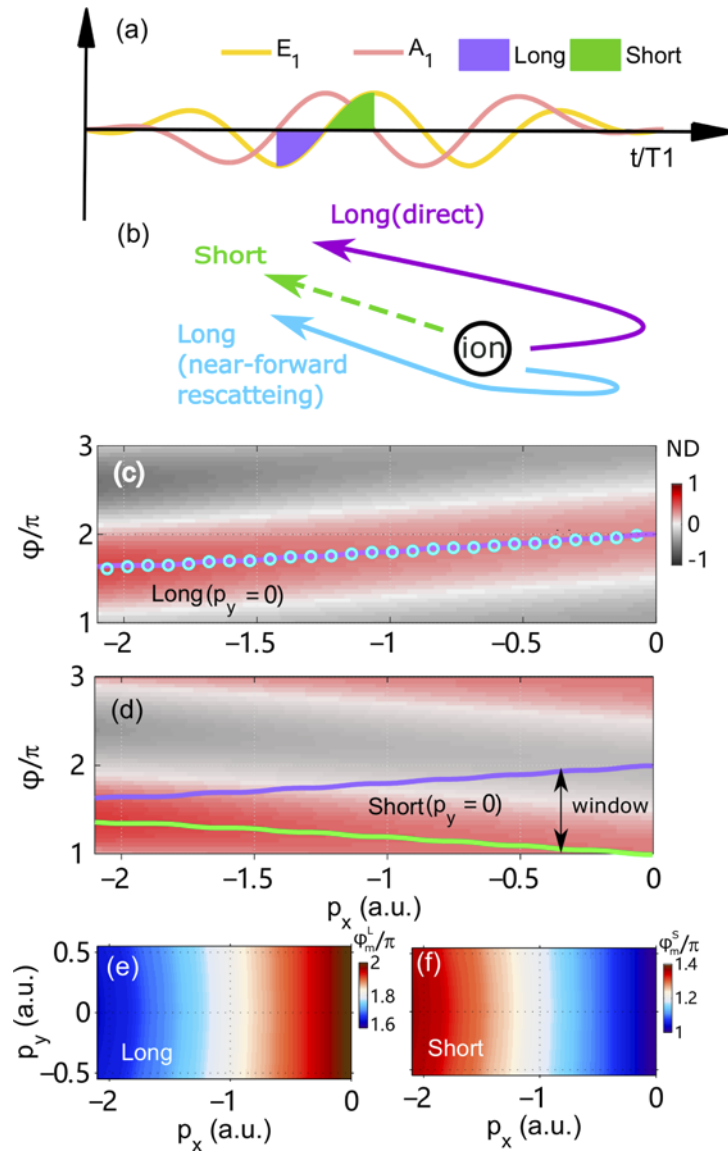


**Fig. 3.** (a) The tunneling ionization times of the long and short trajectories. The yellow curve indicates the electric field of the FM field and the red curve shows its vector potential. (b) The sketch of these electron trajectories. (c) The NDs at the cut of  $p_y = 0$  as functions of  $\varphi$  for the long trajectory. The solid purple curve indicates the phase-of-the-phase of the direct electrons and the blue circles denotes that of the near-forward rescattering electrons. (d) Same as (c) but for the short trajectory (the solid green curve). The solid purple curve indicates the phase-of-the-phase of the long trajectory. The black arrow indicates the phase window formed between  $\varphi_m^L$  and  $\varphi_m^S$ . (e)-(f) The phase-of-the-phase spectra of the long and short trajectories, which are calculated by the SFA, respectively.

and NDs periodically varies with respect to the relative phase, and the relative phase where the variation maximizes suggests us to fit the TDSE results by

$$\cos(\varphi - \varphi_m) = \alpha \cos(\varphi - \varphi_m^L) + \beta \cos(\varphi - \varphi_m^S). \quad (20)$$

Equation (19) implies that  $\alpha$  and  $\beta$  are positive. Hence, according to Eq. (20), the obtained phase  $\varphi_m$  should be located between  $\varphi_m^L$  and  $\varphi_m^S$ , i.e., the phase window. Without the effects of the Coulomb potential, the contributions of these two trajectories are the same, and  $\varphi_m$  equals to the averaged value of  $\varphi_m^L$  and  $\varphi_m^S$  (i.e.,  $1.5\pi$ ) exactly. Based on this point of view, we display two examples of the NDs at  $(p_x, p_y) = (-1.4, -0.2)$  a.u. and  $(p_x, p_y) = (-1.2, 0.2)$  a.u. as functions of the relative phase  $\varphi$  in Figs. 4(a) and 4(b), respectively. Due to the periodicity, we show the result ranging from  $\pi$  to  $3\pi$ . It is shown that the TDSE results of  $\varphi_m$  do not exist at the phase window, which is contrary to our expectations. This is because that in our calculations the Coulomb interaction induced by the electron and target ion has not been taken into account [37,68,72,73]. To contain the effect of the Coulomb potential, in the followings we employ the Coulomb-corrected SFA. In this method, the impacts of the Coulomb interaction on the momentum map are reflected in the ionization times of electron trajectories. In Figs. 5(a)–5(b), we display the ionization times of the long and short trajectories, which are calculated by the SFA and the Coulomb-corrected SFA, respectively. It is shown that including the effects of Coulomb interaction, the ionization times of the long and short trajectories are shifted towards smaller values, and accordingly the phase window is shifted towards a larger  $\varphi$ , as indicated in Figs. 5(c)–5(d). In Figs. 5(e) and 5(f), based on the Coulomb-corrected SFA we show the phase-of-the-phase spectra for the long and short trajectories at each  $\mathbf{p}$ , respectively. Two examples of NDs at  $(p_x, p_y) = (-1.4, -0.2)$  a.u. and  $(p_x, p_y) = (-1.2, 0.2)$  a.u. are displayed in Figs. 4(c) and 4(d). It is indicated that the TDSE result of  $\varphi_m$  lies between the corrected  $\varphi_m^L$  and  $\varphi_m^S$ . For  $(p_x, p_y) = (-1.4, -0.2)$  a.u., it is closer to  $\varphi_m^L$ , and with  $p_x$  increasing, it gets closer and closer to  $\varphi_m^S$ .

In particular, with Eq. (20) we fit the relative contribution ratio  $\alpha/\beta$  of the long and short trajectories, and the obtained  $\varphi_m$  is demonstrated in Fig. 4. In Figs. 4(a) and 4(b), based on SFA the fitted  $\alpha/\beta$  at  $(p_x, p_y) = (-1.4, -0.2)$  a.u. and  $(p_x, p_y) = (-1.2, 0.2)$  a.u. are negative. The results are unreasonable, because  $\alpha$  and  $\beta$  of Eqs. (19) and (20) denote the contributions of the long and short trajectories, and they should be positive. Therefore, when analyzing the relative contribution of long and short trajectories, the SFA is inaccurate. For the results of Coulomb-corrected SFA in Figs. 4(c) and 4(d), the obtained  $\alpha/\beta$  are positive. It implies the effects of the Coulomb interaction on the ionization times of electrons are visible, and they can not be neglected in identifying the contributions of electron trajectories. From Figs. 4(c) and 4(d), it is clearly seen that  $\alpha/\beta > 1$  and at  $(p_x, p_y) = (-1.4, -0.2)$  a.u.,  $\alpha/\beta$  equals 2.95 and at  $(p_x, p_y) = (-1.2, 0.2)$  a.u., it is 1.53. The results indicate that the relative contributions of the long and short trajectories are sensitive to the electron momentum  $\mathbf{p}$ , and the contributions of the long trajectory play as the major roles in the PEMDs.

In Figs. 6(a) and 6(b), we display the ratios  $\alpha/\beta$  for the Coulomb potential and the short-range potential with  $s = 1$  at each  $\mathbf{p}$ . For a better view, several cuts of the ratio are displayed in Figs. 6(c) and 6(d). It is shown that the ratios for the Coulomb potential oscillate between 0.5 and 4, and the amplitude of this oscillation is sensitive to  $\mathbf{p}$ . More interestingly, at the minima of the oscillation,  $\alpha/\beta < 1$ , which indicates that the contributions of the short trajectory is larger than that of the long trajectory. In previous studies, it is often assumed that only the long trajectory contributes to the photoelectron yield. Analyzing the PEMDs, the time information of the electrons from the long trajectories were extracted [36]. Here, our results show the short trajectory also significantly contributes to the PEMDs. For the short-range potential with  $s = 1$ ,  $\alpha/\beta$  is around 1 and its oscillation is not obvious. This implies that the contributions of the long and short trajectories are similar. Increasing the range of the Coulomb interaction ( $s = 10$ ), the results of  $\alpha/\beta$  tend to that of the Coulomb potential.

After strong-field tunneling ionization, the Coulomb interaction seriously affects the electron trajectories. Compared to the short trajectory, the effects on the long trajectory are more evident. This is because that the electrons from the long trajectory may return back to rescatter

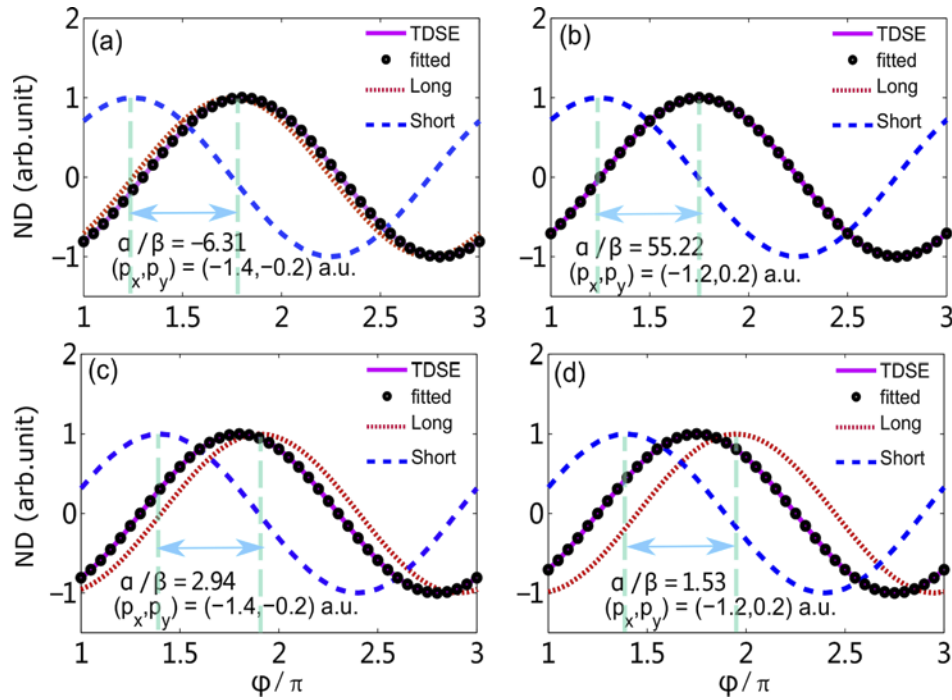


**Fig. 4.** (a) The NDs at  $(p_x, p_y) = (-1.4, -0.2)$  a.u. as functions of  $\varphi$ . The solid purple curve denotes the TDSE results and black dots represent the fitted results. The dashed red and blue curves indicate the data of the long and short trajectories calculated by SFA, and the dashed cyan lines indicate their phase-of-the-phase. The cyan arrow is the phase window formed by  $\varphi_m^L$  and  $\varphi_m^S$ . (b) Same as (a) but for another electron momentum  $(p_x, p_y) = (-1.2, 0.2)$  a.u.. (c) Same as (a), but the NDs of long and short trajectories are obtained from the Coulomb-corrected SFA. (d) Same as (c) but for  $(p_x, p_y) = (-1.2, 0.2)$  a.u..

with the parent ion, leading to the final electron momentum redistribution. Moreover, for the long trajectory, the direct electrons interfere with the rescattering electrons, inducing the holographic interference. At the interference maximum, the electrons interfere constructively, and the contributions of the long trajectory are thus enhanced. While, at the interference minimum, these electrons interfere destructively. Therefore, the contributions of the long trajectory are suppressed, even exceeded by that of the short trajectory. For the short-range potential with  $s = 1$ , the holographic pattern does not exist, and the oscillation in  $\alpha/\beta$  spectrum disappears.

For the momentum region of  $p < 2\sqrt{U_p}$ , the electron mainly undergoes a near-forward rescattering with the parent ion. According to Eq. (18), the rescattering probability of electron is related to the incident momentum  $p'$  and scattering angle  $\theta$ . With three-step model [18], we obtain that  $p'$  and  $\theta$  of near-forward rescattering electron depending on the longitudinal and traverse momenta present a triangular momentum distribution, as displayed in Figs. 7(a) and 7(b), respectively. Outside the triangular momentum region, the multiple-returning backward rescattering electron dominates the contribution of the photoelectron yield [47,54]. In the triangular region, the larger  $|p_x|$  corresponds to the smaller  $|p'|$ , and the larger  $|p_y|$  corresponds to the larger  $|\theta|$ . This means that with  $|p_x|$  increases, the differential scattering cross section of Eq. (18) gradually increases, and thus the contributions of the long trajectory become more and more important, even dominate in PEMDs. While, as  $|p_y|$  increases,  $\sigma$  decreases, and the contributions of the long trajectory are suppressed. It should be noted that at the cut of  $p_x = -1.1$  a.u.,  $\alpha/\beta$  presents a marked increase

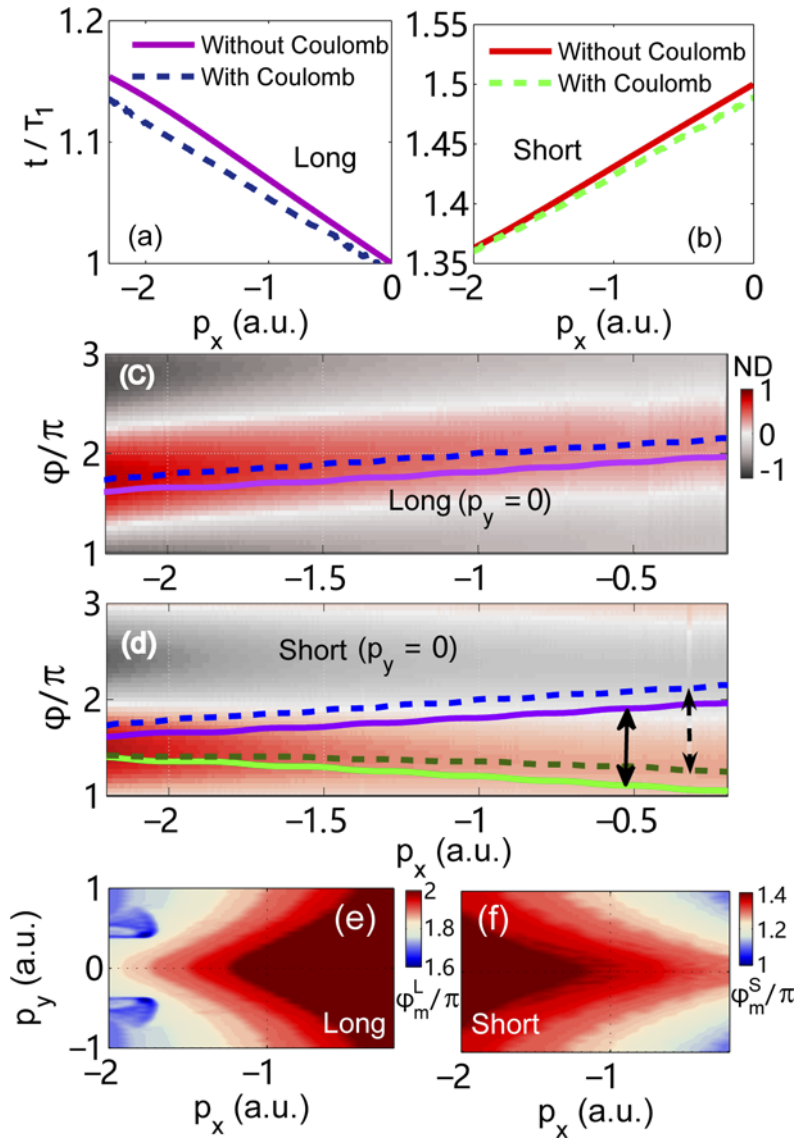


**Fig. 5.** (a)-(b) The ionization times of the long and short trajectories as functions of  $p_x$ . The solid curves indicate the results of Eq. (9) and the dashed curves show the data of Eq. (14). (c)-(d) The NDs obtained from the Coulomb-corrected SFA as functions of  $\varphi$  at the cut of  $p_y = 0$  for the long and short trajectories. The dashed curve shows the phase-of-the-phase of (c)-(d), and the solid curves indicates that extracted from Figs. 3(c)–3(d). The solid black arrow indicates the phase window in Fig. 3(c), and it is shifted toward the dashed arrow here. (e)-(f) The phase-of-the-phase spectra for the long and short trajectories calculated by the Coulomb-corrected SFA, respectively.

for  $|p_y| > 0.4$  a.u., as shown in Fig. 6(c). Moreover, as  $|p_x|$  increases, the momentum  $|p_y|$  where the marked increase occurs, is decreasing. This implies that  $\alpha/\beta$  increase occurs outside the triangular momentum region, and thus it is mainly induced by the multiple-returning backward rescattering electron [74].

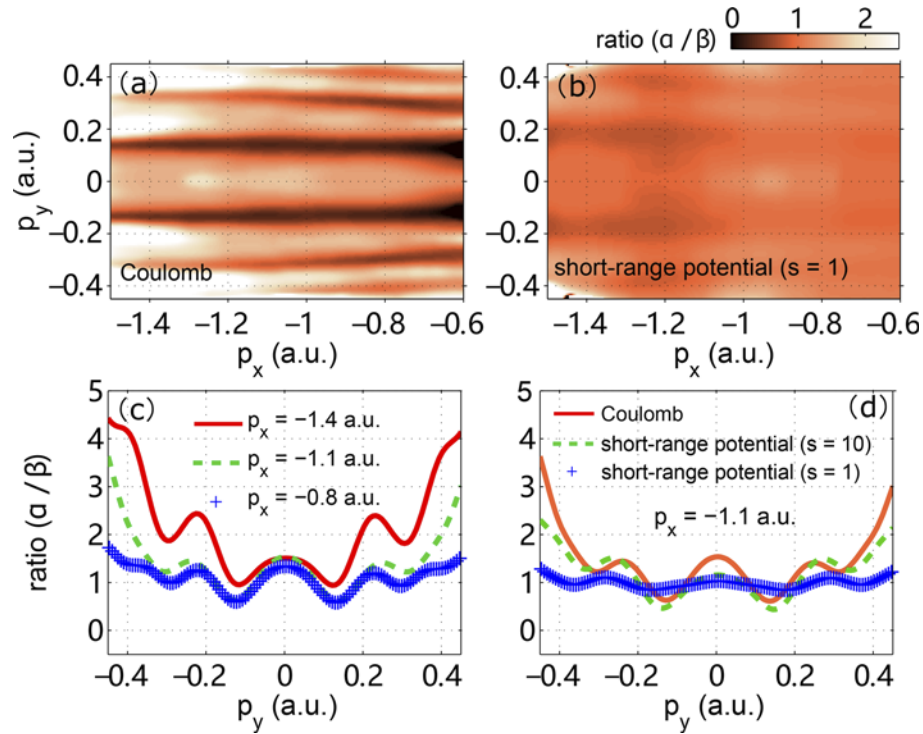


**Fig. 6.** (a)-(b)  $\alpha/\beta$  obtained for the Coulomb potential and the short-range potential with  $s = 1$ , respectively. (c) The cuts of  $\alpha/\beta$  for the Coulomb potential at  $p_x = -0.8$  a.u. (blue crosses),  $-1.1$  a.u. (dashed green curve) and  $-1.4$  a.u. (solid red curve). (d) The cuts of  $\alpha/\beta$  at  $p_x = -1.1$  a.u. for the Coulomb potential (solid red curve), and the short-range potentials with  $s = 10$  (dashed green curve) and  $s = 1$  (blue crosses).

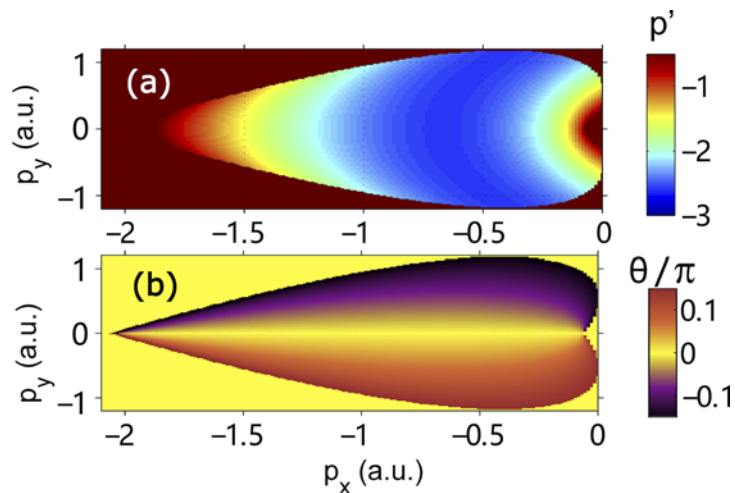


**Fig. 7.** The incident momentum (a) and the scattering angle (b) distributions in the  $(p_x, p_y)$  plane. The laser parameters are the same as that in Fig. 1. Because the weak SH field does not change the incident momentum and scattering angle, and here we show the results in the FM field.

#### 4. Conclusion

In conclusion, with the two-color phase-of-the-phase spectroscopy, we have quantitatively studied the relative contributions of the strong-field tunneling ionization of photoelectrons from the long and short trajectories. Recently, our scheme of weighting the relative contributions of the long and short orbits has been realized in experiment [75]. Here, our work determines the relative contribution, and further explores the dynamics of the oscillation of the relative contribution ratio. The obtained results show that the relative contributions of the electrons from these two trajectories sensitively depend on the final transverse and longitudinal momenta. This is due to the effects of the Coulomb interaction on the long trajectory, which results in the photoelectron momentum and electron trajectories redistribution. Additionally, the near-forward rescattering electrons of the long trajectory interfere with the direct electron leading to the hologram, which greatly strengthens and weakens the contributions of the long trajectory at the interference maxima and minima. Performing the two-color scheme for both the model atoms with the Coulomb potential and the short-range potential, the validity of the scheme and the long-range Coulomb interaction are confirmed. Moreover, our work shows that the effects of the Coulomb interaction on the ionization times of electrons are visible and can not be neglected in identifying the contributions of electron trajectories. This study provides a comprehensive understanding of how the Coulomb potential redistributes the electron momentum and the corresponding quantum orbits in strong-field tunneling ionization, and it will be benefit for the further time-resolved measurements based on photoelectron spectroscopy.

**Funding.** National Key Research and Development Program of China (2019YFA0308300); National Natural Science Foundation of China (11874163, 11934006, 12021004); Natural Science Foundation of Hubei Province (2020CFB362); Hubei Provincial Department of Education (B2020176).

**Acknowledgments.** Numerical simulations presented in this paper were carried out using the High Performance Computing Center experimental testbed in SCTS/CGCL (see <http://grid.hust.edu.cn/hpcc>).

**Disclosures.** The authors declare no conflicts of interest.

**Data availability.** Data underlying the results presented in this paper are not publicly available at this time but may be obtained from the authors upon reasonable request.

#### References

1. G. G. Paulus, W. Nicklich, H. Xu, P. Lambropoulos, and H. Walther, "Plateau in Above Threshold Ionization Spectra," *Phys. Rev. Lett.* **72**(18), 2851–2854 (1994).
2. W. Becker, F. Grasbon, R. Kopold, D. B. Milošević, G. G. Paulus, and H. Walther, "Above-threshold ionization: From classical features to quantum effect," *Adv. At., Mol., Opt. Phys.* **48**, 35–98 (2002).
3. M. Ferray, A. L'Huillier, X. F. Li, L. A. Lompré, G. Mainfray, and C. Manus, "Multiple-harmonic conversion of 1064 nm radiation in rare gases," *J. Phys. B* **21**(3), L31–L35 (1988).
4. J. L. Krause, K. J. Schafer, and K. C. Kulander, "High-order harmonic generation from atoms and ions in the high intensity regime," *Phys. Rev. Lett.* **68**(24), 3535–3538 (1992).
5. B. Walker, B. Sheehy, L. F. DiMauro, P. Agostini, K. J. Schafer, and K. C. Kulander, "Precision measurement of strong field double ionization of helium," *Phys. Rev. Lett.* **73**(9), 1227–1230 (1994).
6. W. Becker, X. J. Liu, P. J. Ho, and J. H. Eberly, "Theories of photoelectron correlation in laser-driven multiple atomic ionization," *Rev. Mod. Phys.* **84**(3), 1011–1043 (2012).
7. Y. Zhou, C. Huang, Q. Liao, and P. Lu, "Classical simulations including electron correlations for sequential double ionization," *Phys. Rev. Lett.* **109**(5), 053004 (2012).
8. G. Sansone, E. Benedetti, F. Calegari, C. Vozzi, L. Avaldi, R. Flammini, L. Poletto, P. Villoresi, C. Altucci, R. Velotta, S. Stagira, S. D. Silvestri, and M. Nisoli, "Isolated single-cycle attosecond pulses," *Science* **314**(5798), 443–446 (2006).
9. E. Goulielmakis, M. Schultze, M. Hofstetter, V. S. Yakovlev, J. Gagnon, M. Uiberacker, A. L. Aquila, E. M. Gullikson, D. T. Attwood, R. Kienberger, F. Krausz, and U. Kleineberg, "Single-cycle nonlinear optics," *Science* **320**(5883), 1614–1617 (2008).
10. T. Gaumnitz, A. Jain, Y. Pertot, M. Huppert, I. Jordan, F. A. Lamas, and H. J. Wörner, "Streaking of 43-attosecond soft-X-ray pulses generated by a passively CEP-stable mid-infrared driver," *Opt. Express* **25**(22), 27506 (2017).
11. J. Li, X. Ren, Y. Yin, K. Zhao, A. Chew, Y. Cheng, E. Cunningham, Y. Wang, S. Hu, Y. Wu, M. Chini, and Z. Chang, "53-attosecond X-ray pulses reach the carbon K-edge," *Nat. Commun.* **8**(1), 186 (2017).
12. J. Itatani, J. Levesque, D. Zeidler, H. Niikura, H. Pépin, J. C. Kieffer, P. B. Corkum, and D. M. Villeneuve, "Tomographic imaging of molecular orbitals," *Nature* **432**(7019), 867–871 (2004).

13. H. Yuan, L. He, F. Wang, B. Wang, X. Zhu, P. Lan, and P. Lu, "Tomography of asymmetric molecular orbits with a one-color inhomogeneous field," *Opt. Lett.* **43**(4), 931 (2018).
14. T. Zuo, A. D. Bandrauk, and P. B. Corkum, "Laser-induced electron diffraction: a new tool for probing ultrafast molecular dynamics," *Chem. Phys. Lett.* **259**(3-4), 313-320 (1996).
15. C. I. Blaga, J. Xu, A. D. DiChiara, E. Sistrunk, K. Zhang, P. Agostini, T. A. Miller, L. F. DiMauro, and C. D. Lin, "Imaging ultrafast molecular dynamics with laser-induced electron diffraction," *Nature* **483**(7388), 194-197 (2012).
16. M. He, Y. Li, Y. Zhou, M. Li, W. Cao, and P. Lu, "Direct Visualization of Valence Electron Motion Using Strong-Field Photoelectron Holography," *Phys. Rev. Lett.* **120**(13), 133204 (2018).
17. P. Salières, B. Carré, L. L. Déroff, F. Grasbon, G. G. Paulus, H. Walther, R. Kopold, W. Becker, D. B. Milošević, A. Sanpera, and M. Lewenstein, "Feynman's path-integral approach for intense-laser-atom interactions," *Science* **292**(5518), 902-905 (2001).
18. P. B. Corkum, "Plasma Perspective on Strong Field Multiphoton Ionization," *Phys. Rev. Lett.* **71**(13), 1994-1997 (1993).
19. S. Baker, J. S. Robinson, C. A. Haworth, H. Teng, R. A. Smith, C. C. Chirilă, M. Lein, J. W. G. Tisch, and J. P. Marangos, "Probing Proton Dynamics in Molecules on an Attosecond Time Scale," *Science* **312**(5772), 424-427 (2006).
20. W. Li, X. Zhou, R. Lock, S. Patchkovskii, A. Stolow, H. Kapteyn, and M. Murnane, "Time-resolved dynamics in N<sub>2</sub>O<sub>4</sub> probed using high harmonic generation," *Science* **322**(5905), 1207-1211 (2008).
21. B. McFarland, J. Farrell, P. Bucksbaum, and M. Guhr, "High harmonic generation from multiple orbitals in N<sub>2</sub>," *Science* **322**(5905), 1232-1235 (2008).
22. O. Smirnova, Y. Mairesse, S. Patchkovskii, N. Dudovich, D. Villeneuve, P. Corkum, and M. Y. Ivanov, "High harmonic interferometry of multi-electron dynamics in molecules," *Nature* **460**(7258), 972-977 (2009).
23. X. Xie, S. Roither, D. Kartashov, E. Persson, D. G. Arbó, L. Zhang, S. Gräfe, M. S. Schöffler, J. Burgdörfer, A. Baltuška, and M. Kitzler, "Attosecond probe of valence-electron wave packets by subcycle sculpted laser fields," *Phys. Rev. Lett.* **108**(19), 193004 (2012).
24. P. Kraus, B. Mignolet, D. Baykusheva, A. Rupenyan, L. Horný, E. Penka, G. Grassi, O. Tolstikhin, J. Schneider, F. Jensen, L. Madsen, A. Bandrauk, F. Remacle, and H. Wörner, "Measurement and laser control of attosecond charge migration in ionized iodoacetylene," *Science* **350**(6262), 790-795 (2015).
25. M. Haertelt, X. Bian, M. Spanner, A. Staudte, and P. Corkum, "Probing molecular dynamics by laser-induced backscattering holography," *Phys. Rev. Lett.* **116**(13), 133001 (2016).
26. P. Lan, M. Ruhmann, L. He, C. Zhai, F. Wang, X. Zhu, Q. Zhang, Y. Zhou, M. Li, M. Lein, and P. Lu, "Attosecond probing of nuclear dynamics with trajectory-resolved high-harmonic spectroscopy," *Phys. Rev. Lett.* **119**(3), 033201 (2017).
27. D. Shafir, H. Soifer, B. D. Bruner, M. Dagan, Y. Mairesse, S. Patchkovskii, M. Y. Ivanov, O. Smirnova, and N. Dudovich, "Resolving the time when an electron exits a tunnelling barrier," *Nature (London)* **485**(7398), 343-346 (2012).
28. J. Tan, Y. Zhou, M. He, Y. Chen, Q. Ke, J. Liang, X. Zhu, M. Li, and P. Lu, "Determination of the Ionization Time Using Attosecond Photoelectron Interferometry," *Phys. Rev. Lett.* **121**(25), 253203 (2018).
29. D. D. Hickstein, P. Ranitovic, S. Witte, X. Tong, Y. Huismans, P. Arpin, X. Zhou, K. E. Keister, C. W. Hogle, B. Zhang, C. Ding, P. Johnsson, N. Toshima, M. J. J. Vrakking, M. M. Murnane, and H. C. Kapteyn, "Direct Visualization of Laser-Driven Electron Multiple Scattering and Tunneling Distance in Strong-Field Ionization," *Phys. Rev. Lett.* **109**(7), 073004 (2012).
30. M. Meckel, A. Staudte, S. Patchkovskii, D. M. Villeneuve, P. B. Corkum, R. Dörner, and M. Spanner, "Signatures of the continuum electron phase in molecular strong-field photoelectron holography," *Nat. Phys.* **10**(8), 594-600 (2014).
31. M. M. Liu, M. Li, C. Wu, Q. Gong, A. Staudte, and Y. Liu, "Phase Structure of Strong-Field Tunneling Wave Packet from Molecules," *Phys. Rev. Lett.* **116**(16), 163004 (2016).
32. B. Xue, Y. Huismans, O. Smirnova, K. Yuan, M. J. J. Vrakking, and A. D. Bandrauk, "Subcycle interference dynamics of time-resolved photoelectron holography with midinfrared laser pulses," *Phys. Rev. A* **84**(4), 043420 (2011).
33. X. Lai, C. Wang, Y. Chen, Z. Hu, W. Quan, and X. Liu, "Elliptical Polarization Favors Long Quantum Orbits in High-Order Above-Threshold Ionization of Noble Gases," *Phys. Rev. Lett.* **110**(4), 043002 (2013).
34. F. Lindner, M. G. Schätzel, H. Walther, A. Baltuška, E. Goulielmakis, F. Krausz, D. B. Milošević, D. Bauer, W. Becker, and G. G. Paulus, "Attosecond double-slit experiment," *Phys. Rev. Lett.* **95**(4), 040401 (2005).
35. D. Arbó, S. Nagele, X. -M. Tong, X. Xie, M. Kitzler, and J. Burgdörfer, "Interference of electron wave packets in atomic ionization by subcycle sculpted laser pulses," *Phys. Rev. A* **89**(4), 043414 (2014).
36. G. Porat, G. Alon, S. Rozen, O. Pedatzur, M. Krüger, D. Azoury, A. Natan, G. Orenstein, B. D. Bruner, M. J. J. Vrakking, and N. Dudovich, "Attosecond time-resolved photoelectron holography," *Nat. Commun.* **9**(1), 2805 (2018).
37. S. Popruzhenko and D. Bauer, "Strong field approximation for systems with Coulomb interaction," *J. Mod. Opt.* **55**(16), 2573-2589 (2008).
38. T. -M. Yan, S. V. Popruzhenko, M. J. J. Vrakking, and D. Bauer, "Low-Energy Structures in Strong Field Ionization Revealed by Quantum Orbits," *Phys. Rev. Lett.* **105**(25), 253002 (2010).
39. Y. Huismans, A. Gijsbertsen, A. S. Smolkowska, J. H. Jungmann, A. Rouzée, P. S. W. M. Logman, F. Lépine, C. Cauchy, S. Zamith, T. Marchenko, J. M. Bakker, G. Berden, B. Redlich, A. F. G. van der Meer, M. Yu. Ivanov, T. -M.



- Yan, D. Bauer, O. Smirnova, and M. J. J. Vrakking, "Scaling laws for photoelectron holography in the midinfrared wavelength regime," *Phys. Rev. Lett.* **109**(1), 013002 (2012).
40. T.-M. Yan and D. Bauer, "Sub-barrier Coulomb effects on the interference pattern in tunneling-ionization photoelectron spectra," *Phys. Rev. A* **86**(5), 053403 (2012).
  41. M. Han, P. Ge, Y. Shao, M. Liu, Y. Deng, C. Wu, Q. Gong, and Y. Liu, "Revealing the Sub-Barrier Phase using a Spatiotemporal Interferometer with Orthogonal Two-Color Laser Fields of Comparable Intensity," *Phys. Rev. Lett.* **119**(7), 073201 (2017).
  42. N. Eicke, S. Brennecke, and M. Lein, "Attosecond-Scale Streaking Methods for Strong-Field Ionization by Tailored Fields," *Phys. Rev. Lett.* **124**(4), 043202 (2020).
  43. J. Henkel and M. Lein, "Analysis of electron trajectories with two-color strong-field ionization," *Phys. Rev. A* **92**(1), 013422 (2015).
  44. N. Eicke and M. Lein, "Extracting trajectory information from two-color strong-field ionization," *J. Mod. Opt.* **64**(10-11), 981–986 (2017).
  45. S. Zherebtsov, F. Süßmann, C. Peltz, J. Plenge, K. J. Betsch, I. Znakovskaya, A. S. Alnaser, N. G. Johnson, M. Kübel, A. Horn, V. Mondes, C. Graf, S. A. Trushin, A. Azzeer, M. J. J. Vrakking, G. G. Paulus, F. Krausz, E. Rühl, T. Fennel, and M. F. Kling, "Carrier-envelope phase-tagged imaging of the controlled electron acceleration from SiO<sub>2</sub> nanospheres in intense few-cycle laser fields," *New J. Phys.* **14**(7), 075010 (2012).
  46. L. J. Zipp, A. Natan, and P. H. Bucksbaum, "Probing electron delays in above-threshold ionization," *Optica* **1**(6), 361–364 (2014).
  47. S. Skruszewicz, J. Tiggesbäumker, K.-H. Meiwes-Broer, M. Arbeiter, T. Fennel, and D. Bauer, "Two-Color Strong-Field Photoelectron Spectroscopy and the Phase of the Phase," *Phys. Rev. Lett.* **115**(4), 043001 (2015).
  48. X. Gong, C. Lin, F. He, Q. Song, K. Lin, Q. Ji, W. Zhang, J. Ma, P. Lu, Y. Liu, H. Zeng, W. Yang, and J. Wu, "Energy-Resolved Ultrashort Delays of Photoelectron Emission Clocked by Orthogonal Two-Color Laser Fields," *Phys. Rev. Lett.* **118**(14), 143203 (2017).
  49. X. Gong, G. Shi, G. Zhang, J. Xu, C. Lin, J. Chen, and W. Yang, "Attosecond Time Delay of Retrapped Resonant Ionization," *Phys. Rev. Lett.* **121**(10), 103201 (2018).
  50. J. Braß, R. Milbradt, S. Villalba-Chávez, G. G. Paulus, and C. Müller, "Two-color phase-of-the-phase spectroscopy applied to nonperturbative electron-positron pair production in strong oscillating electric fields," *Phys. Rev. A* **101**(4), 043401 (2020).
  51. D. Würzler, N. Eicke, M. Möller, D. Seipt, A. M. Saylor, S. Fritzsche, and M. Lein and G. G. Paulus, "Velocity map imaging of scattering dynamics in orthogonal two-color fields," *J. Phys. B: At., Mol. Opt. Phys.* **51**(1), 015001 (2018).
  52. V. A. Tulskey, B. Krebs, J. Tiggesbäumker, and D. Bauer, "Revealing laser-coherent electron features using phase-of-the-phase spectroscopy," *J. Phys. B: At., Mol. Opt. Phys.* **53**(7), 074001 (2020).
  53. M. A. Almajid, M. Zabel, S. Skruszewicz, J. Tiggesbäumker, and D. Bauer, "Two-color phase-of-the-phase spectroscopy in the multiphoton regime," *J. Phys. B: At., Mol. Opt. Phys.* **50**(19), 194001 (2017).
  54. J. Tan, Y. Li, Y. Zhou, M. He, Y. Chen, M. Li, and P. Lu, "Identifying the contributions of multiple-returning recollision orbits in strong-field above-threshold ionization," *Opt. Quant. Electron* **50**(2), 57 (2018).
  55. D. Würzler, S. Skruszewicz, A. M. Saylor, D. Zille, M. Möller, P. Wustelt, Y. Zhang, J. Tiggesbäumker, and G. G. Paulus, "Accurate retrieval of ionization times by means of the phase-of-the-phase spectroscopy, and its limits," *Phys. Rev. A* **101**(3), 033416 (2020).
  56. M. Protopapas, C. H. Keitel, and P. L. Knight, "Atomic physics with super-high intensity lasers," *Rep. Prog. Phys.* **60**(4), 389–486 (1997).
  57. M. D. Feit, J. A. Fleck, and A. Steiger, "Solution of the schrödinger equation by a spectral method," *J. Comput. Phys.* **47**(3), 412–433 (1982).
  58. X. Tong, K. Hino, and N. Toshima, "Phase-dependent atomic ionization in few-cycle intense laser fields," *Phys. Rev. A* **74**(3), 031405 (2006).
  59. X. Tong, S. Watahiki, K. Hino, and N. Toshima, "Numerical observation of the rescattering wave packet in laser-atom interaction," *Phys. Rev. Lett.* **99**(9), 093001 (2007).
  60. S. Chelkowski, C. Foisy, and A. D. Bandrauk, "Electron-nuclear dynamics of multiphoton H<sub>2</sub><sup>+</sup> dissociative ionization intense laser fields," *Phys. Rev. A* **57**(2), 1176–1185 (1998).
  61. P. He, N. Takemoto, and F. He, "Photoelectron momentum distribution of atomic and molecular systems in strong circularly or elliptically polarized laser field," *Phys. Rev. A* **91**(6), 063413 (2015).
  62. D. B. Milošević, G. G. Paulus, D. Bauer, and W. Becker, "Above-threshold ionization by few-cycle pulses," *J. Phys. B* **39**(14), R203–R262 (2006).
  63. A. M. Perelomov and V. S. Popov, "The Coulomb singularity is regularized through matching to the field-free initial-state wave function, Popov," *Sov. Phys. JETP* **25**, 336 (1967).
  64. Y. Huismans, A. Rouzée, A. Gijsbertsen, J. Jungmann, A. Smolkowska, P. Logman, F. Lépine, C. Cauchy, S. Zamith, T. Marchenko, J. Bakker, G. Berden, B. Redlich, A. van der Meer, H. Muller, W. Vermin, K. Schafer, M. Spanner, M. Ivanov, O. Smirnova, D. Bauer, S. Popruzhenko, and M. Vrakking, "Time-resolved holography with photoelectrons," *Science* **331**(6013), 61–64 (2011).
  65. N. I. Shvetsov-Shilovski, M. Lein, L. B. Madsen, E. Räsänen, Lemell, J. Burgdörfer, D. G. Arbó, and K. Tökési, "Semiclassical two-step model for strong-field ionization," *Phys. Rev. A* **94**(1), 013415 (2016).

66. P. Agostini, F. Fabre, G. Mainfray, G. Petite, and N. K. Rahman, "Free-Free Transitions Following Six-Photon Ionization of Xenon Atoms," *Phys. Rev. Lett.* **42**(17), 1127–1130 (1979).
67. Y. Feng, M. Li, S. Luo, K. Liu, B. Du, Y. Zhou, and P. Lu, "Semiclassical analysis of photoelectron interference in a synthesized two-color laser pulse," *Phys. Rev. A* **100**(6), 063411 (2019).
68. Y. Zhou, O. I. Tolstikhin, and T. Morishita, "Near-forward rescattering photoelectron holography in strong-field ionization: extraction of the phase of the scattering amplitude," *Phys. Rev. Lett.* **116**(17), 173001 (2016).
69. Y. Zhou, J. Tan, M. Li, and P. Lu, "Probing the launching position of the electron wave packet in molecule strong-field tunneling ionization," *Sci. China: Phys., Mech. Astron.* **64**(7), 273011 (2021).
70. W. Yang, H. Zhang, C. Lin, J. Xu, Z. Sheng, X. Song, S. Hu, and J. Chen, "Momentum mapping of continuum-electron wave-packet interference," *Phys. Rev. A* **94**(4), 043419 (2016).
71. E. Rutherford, "LXXIX. The scattering of  $\alpha$  and  $\beta$  particles by matter and the structure of the atom," *Phil. Mag.* **21**(125), 669–688 (1911).
72. P. A. Korneev, S. V. Popruzhenko, S. P. Goreslavski, T.-M. Yan, D. Bauer, W. Becker, M. Kübel, M. F. Kling, C. Rödel, M. Wünsche, and G. G. Paulus, "Interference Carpets in Above-Threshold Ionization: From the Coulomb-Free to the Coulomb-Dominated Regime," *Phys. Rev. Lett.* **108**(22), 223601 (2012).
73. D. G. Arbó, "The effect of the Coulomb potential on subcycle interference of electron wave packets in atomic ionization by two-color laser pulses," *J. Phys. B: At., Mol. Opt. Phys.* **47**(20), 204008 (2014).
74. M. Möller, F. Meyer, A. M. Saylor, G. G. Paulus, M. F. Kling, B. E. Schmidt, W. Becker, and D. B. Milošević, "Off-axis low-energy structures in above-threshold ionization," *Phys. Rev. A* **90**(2), 023412 (2014).
75. J. Tan, S. Xu, X. Han, Y. Zhou, M. Li, W. Cao, Q. Zhang, and P. Lu, "Resolving and Weighing the Quantum Orbits in Strong-Field Tunneling Ionization," *Adv. Photonics* **3**(3), 035001 (2021).